MEMS-based low-cost and open-source accelerograph for earthquake strong-motion

M. A. Bravo-Haro*, X. Ding & A.Y. Elghazouli

Department of Civil and Environmental Engineering, Imperial College London, UK
*Corresponding author: mab214@imperial.ac.uk

Abstract

This paper describes a sensing technique that has been entirely built from off-the-shelf electronic components, with the aim of providing its construction and programming guidelines as an open-source platform which can be continuously updated. The assessments carried out in this investigation indicate that the proposed sensor is suitable for deployment as an accelerograph for seismic monitoring of structural systems. The results show low levels of self- noise, considering the nature of the MEMS analogue accelerometer embedded in the sensor. The amplitude transfer functions exhibit a flat behaviour for the full range of frequencies tested, whose boundaries were limited by the installed capacity within the laboratory. However, this flat behaviour is expected to be coherent up to the resonant frequency of the MEMS accelerometer, whose absolute value is much higher than the bandwidth of frequencies of interest for seismologists and structural earthquake engineers. The clipping tests demonstrate a high linearity, of the amplitude transfer function from low acceleration levels, up to the vicinity of the maximum nominal recordable acceleration of ±3g, at which a typical roll-off is observed. Under long-time operations, the sensor produces a robust performance, maintaining a steady pace of sampling. The performance of the sensor was finally tested considering non-stationary signals, using a linear shake table to reproduce a wide ensemble of strong-motion recordings from actual earthquakes. Intensity measures of strong-motion commonly used in earthquake engineering were appraised, such as horizontal spectral acceleration, Arias Intensity, and transient peaks of response.

1 Introduction

The ever-increasing precision and ever-decreasing cost of Micro Electro-Mechanical Systems (MEMS), especially MEMS accelerometers, have enabled their implementation in a variety of industrial and scientific fields, serving a wide range of tasks that were usually solved by traditionally expensive and large devices. In the realm of seismology and earthquake engineering, MEMS accelerometers, able to record ground accelerations produced by earthquakes, have resulted in several prototypes of low-cost sensors and subsequent arrangement of seismic networks completely based on MEMS sensors. This has been recently referred to as a 'revolution in seismic detection technology' [1] that may transform earthquake science due to the affordability of the sensors themselves and the maintenance of a network of this nature, among others. Early experiences include 'The Quake-Catcher Network' where MEMS accelerometers, able to detect vibrations within 0.1-20 Hz and accelerations usually within $\pm 2g$, behave as a strong-motion seismic station [2, 3]. Another similar network is the 'Home Seismometer for Earthquake Early Warnings', initiated by the Japan Meteorological Agency, where a tri-axial in-house MEMS sensor is used, able to record ground accelerations within a range of $\pm 2g$ at 500 Hz (i.e., 500 samples per second) [4]. More recent examples include 'The Palert Network of Taiwan' for early earthquake warning, whose MEMS sensors record ground accelerations within $\pm 2g$ at 100 samples per second [5]. The first European Urban Seismic Network was developed in Acireale, Italy [6], in addition to pioneering local arrays of accelerographs developed in Lefkada, Greece [7]. It is also worth noting the exploration of MEMS accelerometers embedded in smartphones, either used as fixed sensors, as in the United States Geological Survey (USGS) project for earthquake and tsunami early warning system deployed in Chile [8], or as freely moving devices where human-induced sources of acceleration such as walking, are identified and removed from quake-induced accelerations powered by machine learning methods [9]. Ultimately, the performance of a Raspberry Shake 4D low-cost seismograph and accelerometer [10] was recently shown to be good enough to use as a sensor to densify regional networks designed for studies of local and regional events [11]. Therefore, as discussed above, the potential of MEMS accelerometers for the measurement of ground motion induced by earthquakes has been demonstrated and documented internationally.

Similar to earthquake studies in seismology, structural engineering has also begun to consider using MEMs-based sensors to investigate the motions of buildings. Nonetheless, several differences need to be accounted for, with the range of the amplitude of the accelerations being one of the most significant. For instance, the Community Seismic Network [2] has been instrumenting buildings in California, USA, using the same sensor described above initially designed to record free-field strong-motion at the ground level. The low-cost of the sensors and their maintenance have enabled unprecedented dense arrays in tall buildings, when compared to existing instrumented buildings (e.g., [12, 13]). Moreover, sensors based on MEMS accelerometers have been developed in Structural Health Monitoring (SHM), for tracking various structural typologies and sorting different needs, such as in bridges [14, 15, 16, 17]; and powered by different sensors [18, 19, 20].

In order to illustrate some key aspects that differentiate the peak ground acceleration (PGA) and the response acceleration of a structure, Figure 1 shows the 5%-damped elastic response spectra of two recordings from recent earthquakes in Chile (2010) and Mexico (2017), respectively. The response spectrum provides a summary of the peak response of all possible linear single-degree-of-freedom systems when subjected to a particular component of ground motion [21]. It can be observed here that the maximum acceleration experienced by a wide range of structural systems (i.e., different periods of vibration), is significantly higher than the PGA (i.e., period equal to zero), normally recorded by strong-motion seismic stations. In spite of the dissimilar characteristics of both recordings, in terms of seismogenesis and soil conditions, it is interesting to observe the ratios between the peak acceleration experienced by the structure and the PGA, whose values attain 5.10 and 5.31 for the Maule and Puebla recordings respectively, for a 5%-damped spectral response. Therefore, when significant values of PGA are recorded, as for instance, in the case of the Maule Earthquake recording (Figure 1a) whose PGA is equal to 0.697g, a building might undergo a peak acceleration of 3.549g, if the fundamental period of vibration is tuned to 0.17s. This level of acceleration is typically higher than the maximum range or clipping level of existing MEMS accelerometers or strong-motion seismic stations. In addition, it is important to mention that strength reduction factors are frequently applied to the elastic spectrum, and therefore lower design forces are considered for structural design, mostly due to the inelastic deformations allowed to take place in the structural system. However, focusing the attention in the peak structural response exhibited by the roof of a multi-storey building, response accelerations up to 18 times higher than the PGA might be attained [22], increasing even further in the case of sensitive non-structural elements that are placed within the floor.

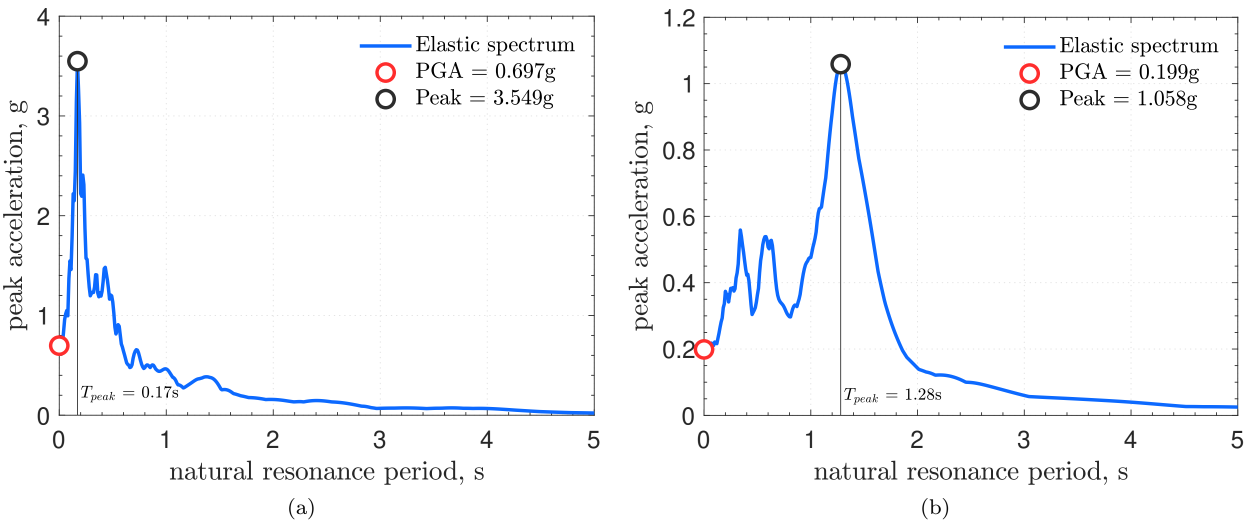

Figure 1: (a) Elastic response spectrum from the 2010 Maule Earthquake in Chile, $M_w = 8.8$, Channel 1, E-W, Angol station. (b) Elastic response spectrum from the 2017 Puebla Earthquake in Mexico, $M_w = 7.1$, Channel 1, N-E, JC54 station. Damping ratio of 0.05 for both spectra.

This paper presents an assessment of the performance of an open-source low-cost accelerograph, built with off-the-shelf electronic components. This is executed throughout standard tests and metrics commonly employed to evaluate the performance of sensors for measuring vibrations, such as seismographs [23]. Suggestions for further development of the sensor are drawn, towards real-time data collection, connectivity, power supply possibilities, and general maintenance of a fully operational sensor.

2 Methodology

2.1 Stationary input motion

In order to enable the use of a sensor as a reliable recorder of induced accelerations, it is essential to understand the behaviour of the final configuration of the device, which usually comprises a MEMS accelerometer attached to a Micro-Controller or to a small Motherboard, in addition to wiring, batteries, and often other sensors to collect additional information (e.g., humidity, temperature). For these type of sensors, individual characterisations are recommended, given that sensors with identical off-the-shelf electronic components, produced by the same manufacturer, may exhibit different performance [6]. Hence, if possible, in the case of MEMS sensors this variability should be taken into account and not only for specific aspects, such as the self-noise, but as thorough as possible (e.g., transfer functions under dynamic inputs, etc).

To characterise the actual performance of an accelerograph based on a MEMS accelerometer, standardised tests are undertaken, as listed below:

1. Self-noise test, to determine the lowest limit of accelerations that the sensor is capable of recording under normal conditions.
2. Box flip test, to observe potential offset and to estimate the static sensitivity of the sensor.
3. Dynamic sine waveform inputs, to build amplitude transfer functions.
4. Dynamic sine waveform inputs, to determine the highest bound of acceleration, or clipping levels, in addition to sensor linearity.
5. Single and double integration test to recover mostly transient time-histories of velocity and displacement.

Dynamic tests were performed herein using a linear servo-controlled actuator, by attaching the sensors to the head of the jack. In addition, for these dynamic tests, a high-accuracy commercial accelerometer (model: PCB ICP 393B04) was used to obtain an individual reference of the output signal of the actuator. This represents vital standard practice that, besides ascertaining the actual response of the mechanical system used for the tests, helps to identify external sources of mechanically-induced noise. As discussed further below, the linear actuator used for the tests, introduces some mechanical noise, in addition to some spurious behaviour in the closed-loop feedback of the control system, mostly at the peaks of the sine wave, for high levels of induced acceleration. Hence, the maximum reliable frequency attained by the linear actuator was 17 Hz for sine waves with low amplitudes, which defines the maximum frequency tested and used for the construction of the amplitude transfers functions of the sensor. To gain insight on the robustness and variability of the proposed sensor's response, two identical prototypes (i.e. same electronic configuration) are subjected to the set of dynamic input motion test (i.e., test 3 and 4).

2.2 Non-stationary input motion

A set of 52 earthquake strong-motion recordings are used to carry out dynamic analysis in a shake table, and are then measured by the prototyped sensor and the standard commercial accelerometer described above. The records were selected to have a wide range of key features, such as: PGA, peak acceleration, duration and energy content. To facilitate the interpretation of results, the suite of records is divided into three sets grouped as: far-field records, near-field with velocity pulses and near-field with no velocity pulses. A full description of the characteristics of the recordings is presented in Section 5.1 and the recorded data are utilised to undertake the following quantitative and qualitative assessments:

1. Accuracy assessment of the raw recorded acceleration signal, as well as velocity and displacement signals obtained by integration of the processed recorded acceleration.
2. Error in the computation of Fourier Amplitude Spectra (FAS).
3. Precision of the 5% damped acceleration response spectrum computed using the recorded acceleration signal.
4. Error in the computation of Arias Intensity (I_A) computed using the recorded acceleration signal.
5. Reliability, robustness and bias of recorded data.

3 Characteristics of the Sensor

This paper presents only one prototyped sensor configuration, based on an open-source Arduino UNO micro-controller and a 3-axis analogue MEMS Adafruit accelerometer ADXL 335, whose characteristics are shown in Table 1. This arrangement of elements has been selected due to its simplicity and robustness compared to several other prototypes tested during this study. The simplicity can be appreciated in Figure 2 where a schematic configuration of the sensor is drawn, and the robustness is judged by several factors, such as the quality of the recorded data due to the timestamp stability of the sampling, or the steady uninterrupted continuous operation during long-time recording tests as presented below in detail. The micro-controller nature of the Arduino board enables the execution of loops and feedback with a high level of precision, making it suitable as a data acquisition (DAQ) system. The total cost of the sensor components, including: micro-controller, MEMS accelerometer, Li-Po battery, case, and cables; amounts to less than £100. It is important to note that although the clipping limit (i.e., $\pm 3g$) of the chosen ADXL 335 MEMS accelerometer is not particularly high, it was selected to be consistent with the limitations of the laboratory testing equipment employed (i.e., dynamic actuator and linear shake-table), and serves to examine the concept and methodology adopted. Figure 3 shows a modified configuration of the sensor that was used during the tests in order to facilitate the data acquisition process, in addition to offering access to the microcontroller during the tests. As shown in the figure, the MEMS accelerometer is wired and encased out of the box to be attached to the linear actuator.

Interestingly, there are other configurations, although not included in this study, but that may offer powerful capabilities to a sensor of this nature, and could be the subject of further consideration. These include the use of a Raspberry Pi single-board micro-computer, that offers the whole environment of an operating system, among peripheral ports and embedded sensors, such as LAN and/or wireless connectivity for transferring recorded data. A Raspberry Pi can be used as replacement of an Arduino board, or jointly in order to exploit the micro-controller quality of the latter and hence reducing the overheads in the Raspberry. This configuration was found to be ideal because when a Raspberry Pi is used alone as the DAQ, 3-component sample rates are limited to 100 samples per second. In addition, several MEMS accelerometer options were tested as well, given the wide range of off-the-shelf, low-cost devices. Here, the most significant difference rests in the analogue or digital nature of the sensor. In the latter case, such as the digital ADXL 326 MEMS accelerometer explored within the study, the analogue-to-digital converter is embedded in the accelerometer and allows different pre-defined ranges of maximum recordable acceleration, up to $\pm 16g$, where the sensitivity drops as the acceleration range increases. However, because the Arduino board can be easily configured to log voltages at 10-bit resolution, we selected the analog ADXL 335 accelerometer for use in our proposed accelerograph.

For this prototype, various levels of sampling rates were considered, where the performance sought is the stability of the timestamp at each recorded sample or, in other words, that the differential of time between consecutive samples has to be constant. In addition, this needs to hold true for longer windows of time, where usually the final timestamp is lagged due to the error accumulation. This is of particular importance in order to record reasonable waveform and thus avoid distortions in the spectral analyses. It was found that the Arduino board is capable of recording three input channels at 400 samples per second, plus a timestamp mark. It is interesting to note that if only one axis of the accelerometer is recorded, 1000 samples per second can be attained with robust performance. However, the capability of recording 3-axis at the same time is appealing for a sensor as this, coupled with the fact that the range of frequencies of interest is much lower than the Nyquist frequency of the rates just mentioned above. As a result, the recorded accelerations during the tests undertaken for this research are fixed at a rate of 200 samples per second. In contrast, the commercial transducer used to compare and validate the results is fixed at a rate of 1000 samples per second, due to the capacity of the sensor and the data acquisition system used to handle it (i.e., National Instruments NI-9234 vibration input mode).

Table 1: MEMS accelerometer nominal characteristics

Parameter	Nominal value
Nominal Maximum acceleration	$\pm 3g$
Bandwidth for X and Y axis	$1600Hz$
Bandwidth for Z axis	$550Hz$
Acceleration sensitivity	$300mV/g \pm 30$
Noise Density X and Y axis	$150\mu g/\sqrt{Hz}\ rms$
Noise Density Z axis	$300\mu g/\sqrt{Hz}\ rms$
Sensor Resonant Frequency	$5.5kHz$

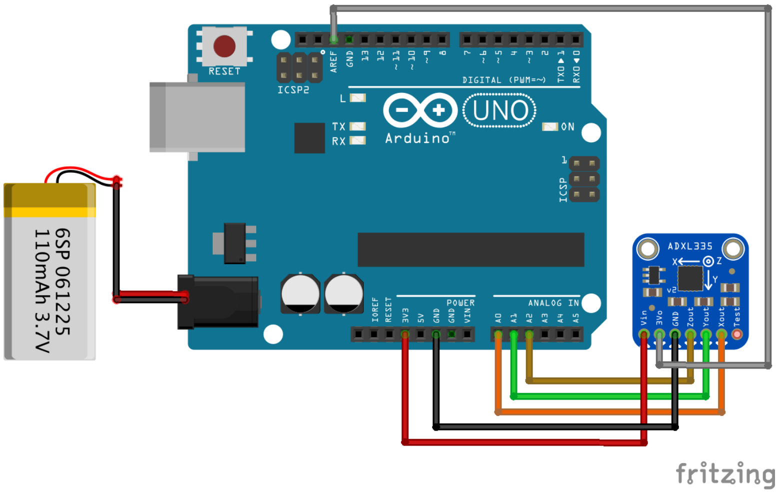

Figure 2: Schematic configuration of the sensor and general wiring between the Arduino board and the MEMS accelerometer.

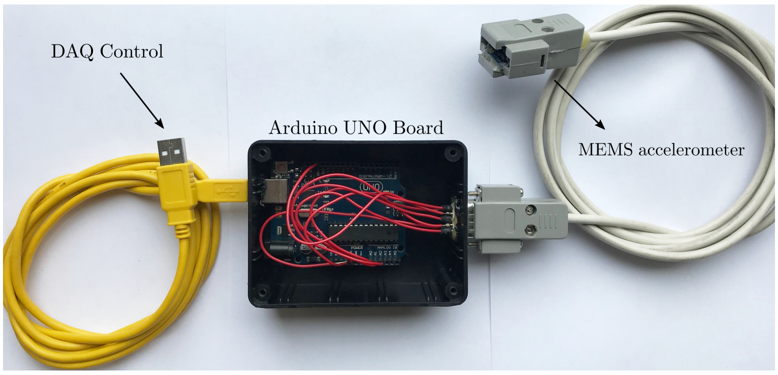

Figure 3: Sensor configuration used during the tests to facilitate the collection of data and final experimental setup.

4 General Performance of the Prototyped Sensor

4.1 Sensor Self-noise

The level of inherent noise produced by the sensor enables the estimation of the weakest motion signal that can be recorded by the device [24]. There are several methods to quantify the self-noise of a sensor, yet for this research the Power Spectral Density (PSD) method is selected. On the one hand, the PSD is formally defined as shown in Equation 1 as follows

$$S_{xx} = \int_{-\infty}^{-\infty} R_{xx}(\tau) e^{-iw\tau} d\tau \tag{1}$$

Where S_{xx} is the two-side PSD of the signal $x(t)$ and R_{xx} is the auto-correlation function of the signal. The self-noise of the MEMs accelerometer as a function of frequency was attained by taking the PSD of 12 hours of data recorded by our system, as shown in Figure 4 for all 3-axes. It was assumed that the PSD of an ambient ground motion signal was suitable low to characterise the overall system self-noise of a low-cost sensor to be used exclusively for recording strong-motion acceleration signals, such as those considered in Section 5.

The acceleration PSD curves are shown in Figure 5 based on data collected with sensor 1. These were calculated using the Welch method [25], using 32 Hanning windows and an 50% overlap within these, which were set based on sensitivity tests. In general, the three axes present a similar response and shape across the frequency range. However, this trend remains valid for the bandwidth of frequencies higher than about 1.0 Hz since, for lower frequencies, axis Z shows a 4 to 5 times higher acceleration PSD with respect to convergent behaviour of axes X and Y. The typical specifications for RMS noise given by the manufacturer (see Table 1) are shown in dashed lines. In the relevant bandwidth of frequencies for earthquake engineering ($\sim 0.2s - 20s$), the three

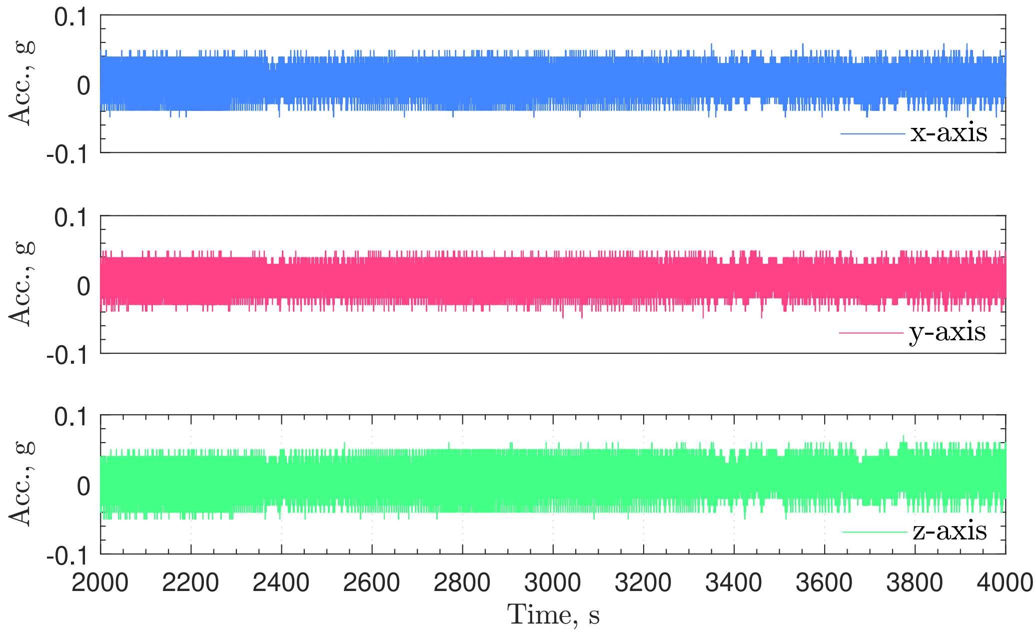

Figure 4: Excerpt of a 12 hours continuous recording under no excitation of the sensor, for all three axes of the MEMS accelerometer.

axes show a relatively low self-noise PSD with respect to signals produced by moderate earthquakes (i.e., good signal-to-noise ratio), hence enabling signal recording [26, 27]. The PSD displayed in Figure 5 are averaged smoothed values estimated using a 10-point and 20-point mean moving algorithm, for frequencies lower and higher than 1.0 Hz, respectively.

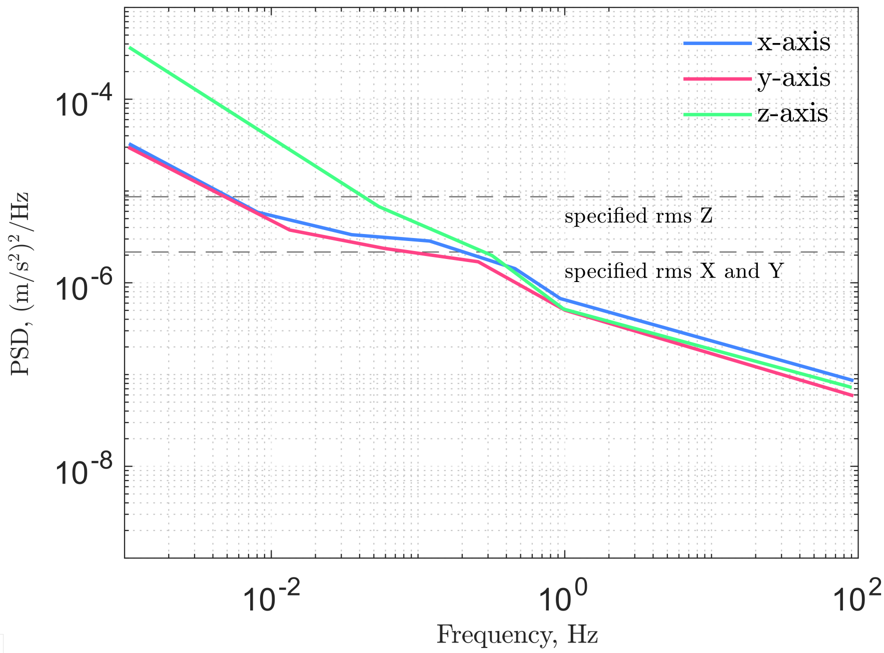

Figure 5: Averaged power spectral density of the acceleration recorded through 12 hours of motionless state of the sensor, for every axis of MEMS accelerometer. Dashed lines show the RMS noise values provided by the manufacturer.

Additionally, the 12 hours long samples were used to observe potential offsets or drifting over time, which were estimated as the average of the signal $x(t)$ over the window of time. The average of the 12 hours recording for each individual axis are: 0.180 m/s^2, 0.088 m/s^2, and 0.118 m/s^2 $(-1g)$ for X, Y, and Z axes, respectively. Correspondingly, the standard deviations per axis are: 1.441x10$-$3 m/s^2, 2.848x10$-$3 m/s^2, and 3.087x10$-$3 m/s^2 for X, Y, and Z axis, respectively. It is important to note that the measured average in all axis is steady through time, and no irregular trends or time-dependant increasing average values are observed, enabling the removal or detrending of these permanent offsets to calibrate the sensor. Additionally, the maximum absolute acceleration of this input signal reached $0.06g$. Finally, it should be noted that further self-noise tests on several sensors would be needed in order to enable a more statistically refined assessment of the comparative reliability and variability of the specific sensor response.

4.2 Box-flip tests

To appraise offset, axis orientation and static or $0Hz$ sensitivity of the sensor, a box-flip test was carried out. Herein, the sensor is accommodated in a cubic box in such a way that the direction of axis of the MEMS accelerometer are parallel to the edges of the box. This enables flipping of the box in turn through the 6 possible positions, in order to use the gravitational acceleration as a reference for all axis in the upward and downward orientation. Theoretically, this method allows estimation of the static sensitivity, offset, and orientation of every axis, along with potential accumulated drifts once the box is set to the initial position [28]. Commonly, a measure of the Earth's static field (e.g., by using an absolute gravimeter) is used as a reference to estimate the difference with the values recorded by the sensor. However, due to the unavailability of this measure, a referential value of g equal to 9.806 m/s^2 is used herein and the test is repeated 10 times, in order to assess the variability of recorded values.

Figure 6 shows a full sequence of one of the box-flip tests based on the performance of sensor 1. Sequentially from left to right, the orientation of the sensor is shown for the static position in the top plot. The perturbations of the signal in between the static positions are due to the transient movement of the box to attain the next position. A median of the values recorded during the zero movement window, bounded by the dashed vertical lines, was used to compute the sensitivity and variability of the sensor. Additionally, negligible drifts are observed at the end of the sequence with respect to the initial measure at the beginning of the test. The latter is crucial to accurately retrieve displacements through double-integration of the acceleration recording, as shown and discussed below in Section 4.5.

The computed static sensitivity, which can be seen as the slope of the calibration curve, is on average over the three axes equal to $316.36mV/g$. This value is in close agreement with the typical sensitivity reported by the manufacturer, which is $300mV/g \pm 30$. This was estimated using directly the raw data recorded during the zero movement window within the box-flip test. It is noteworthy that low-cost commercially available MEMS accelerometers are becoming more precise, even when compared with recently reported static sensitivity levels [28].

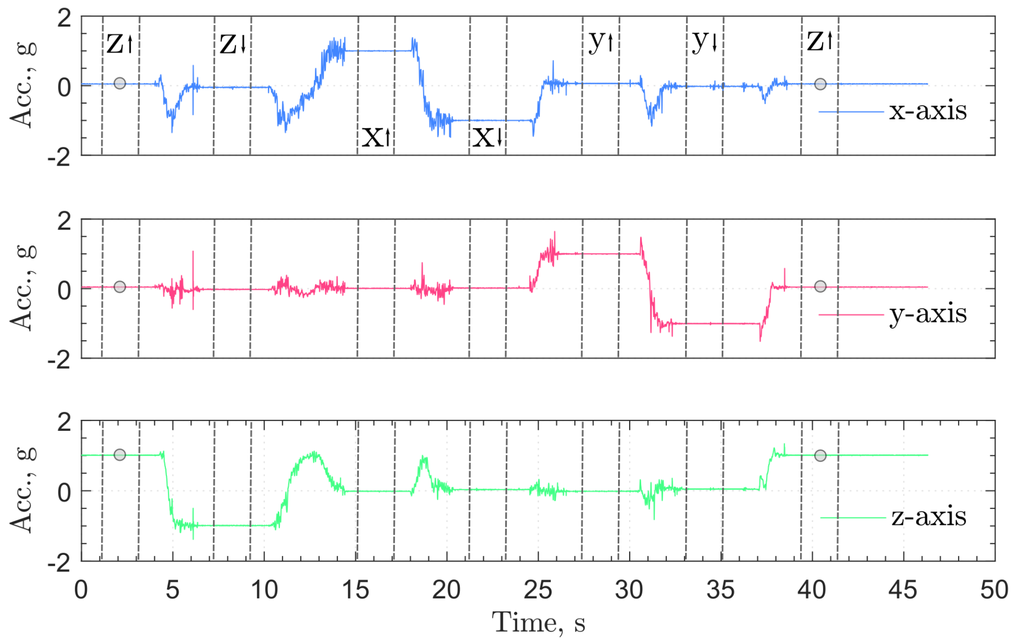

Figure 6: Flip box test based on raw data recorded by the sensor. The sequence of positions of the sensor during the test are shown at the top plot, where the arrow indicates the upward and downward position of the axis with respect to a flat surface.

4.3 Transfer function tests

A transfer function is the ratio of the output to the input of the system. In this case, it relates the amplitude and the phase of the input signal applied to the dynamic jack to that recorded by the sensor. The attention is herein focused on estimating the ratio of the amplitude response for a wide range of signals with different frequencies, in order to establish the range of "flat-response" of the sensor. Towards this aim, a uniaxial dynamic actuator was used to input sinusoidal waves with several amplitudes and frequencies, which were recorded at the same time by the MEMS sensor and the transducer. As mentioned above, the input signal (i.e. ideal synthetic signal) followed by the control system of the dynamic actuator, differs from the end actual performance of the jack, hence the information recorded by the high fidelity transducer is used as a reference in the forthcoming analyses.

The computation of the amplitude ratios can be performed directly on the time-domain by a root-mean-square (RMS) of the recorded accelerations, or it can be carried out on the frequency-domain through a spectral analysis. The main shortcoming of the former is the sensitivity of the RMS to noise from different sources that are captured by the sensor [28], especially in the case of low frequency weak signals, that demand the maximum length of the actuator stroke to achieve a minimum level of excitation in terms of acceleration, thus external and internal noise is overcome. The latter spectral method is instead used in this study due to its robustness and accuracy, and also because the recording sampling rate of the sensor is highly steady enabling frequency-domain analyses. The methodology presented by [28] is followed to compute the total power of the dominant frequencies of the signal. This is illustrated in Figure 7 and Figure 8 for a sine wave input with 10mm and 5Hz of nominal amplitude and frequency respectively.

Figure 7 shows an excerpt of the measured acceleration by the MEMS sensor and the transducer, in addition to the synthetic input signal, whose total response, of approximately 20s of duration, is then used in the spectral analysis presented in Figure 8. The power of the signal is computed in a narrow band around the peak of the dominant frequency which for the case of the sensor usually matches the reference input frequency; this enables filtering-out the noise carried by frequencies out of the limits of the narrow band. To define this band, the 5 frequency points around the peak amplitudes reported by the sensor are used, and their FFT amplitudes are employed to render a unique acceleration value through the root-mean square method.

Before discussing the amplitude ratios obtained from all wave sine input signals considered in the test, it is worth noting that the sampling ratio of the sensor is fixed to 200 samples per seconds, whereas the transducer is sampling at 1000 samples per second, given the capability of the DAQ system reported above. By using the raw data of the transducer, a precise match of the synthetic sine wave input to the actuator is attained, as shown in Figure 8.

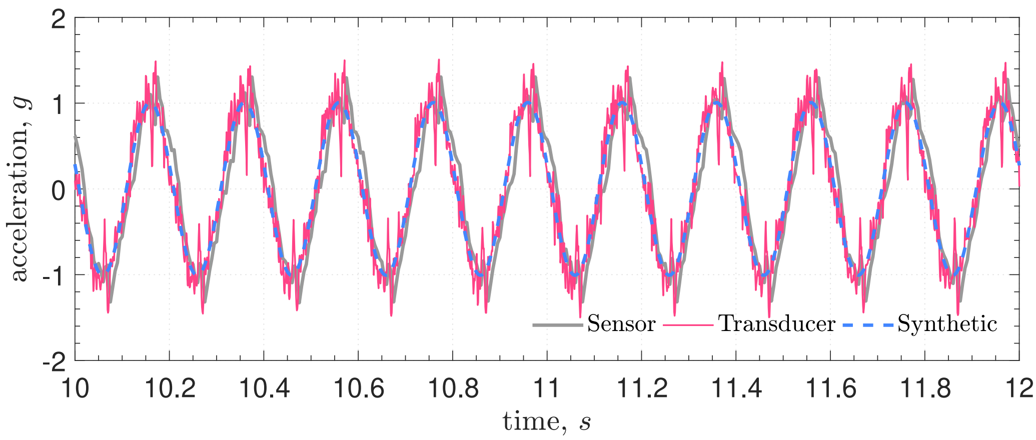

Figure 7: Excerpt of raw data from a sinusoidal input signal of 10 mm nominal amplitude and 5 Hz nominal frequency.

By computing the amplitude ratios, using the spectral method on the input signals tested in the linear actuator, the amplitude frequency response of the sensors can be obtained, as shown in Figure 9, for all axes of the MEMS accelerometer. Specifically, 24 sine waves were considered, ranging from $0.1Hz$ to $0.5Hz$ with intervals of $0.1Hz$, and from $1Hz$ to $17Hz$ with intervals of $1Hz$. In general, the amplitude ratio shows a good behaviour, given the flatness of the amplitude response for the whole range of tested frequencies, which were limited by the mechanical capacity of the linear actuator.

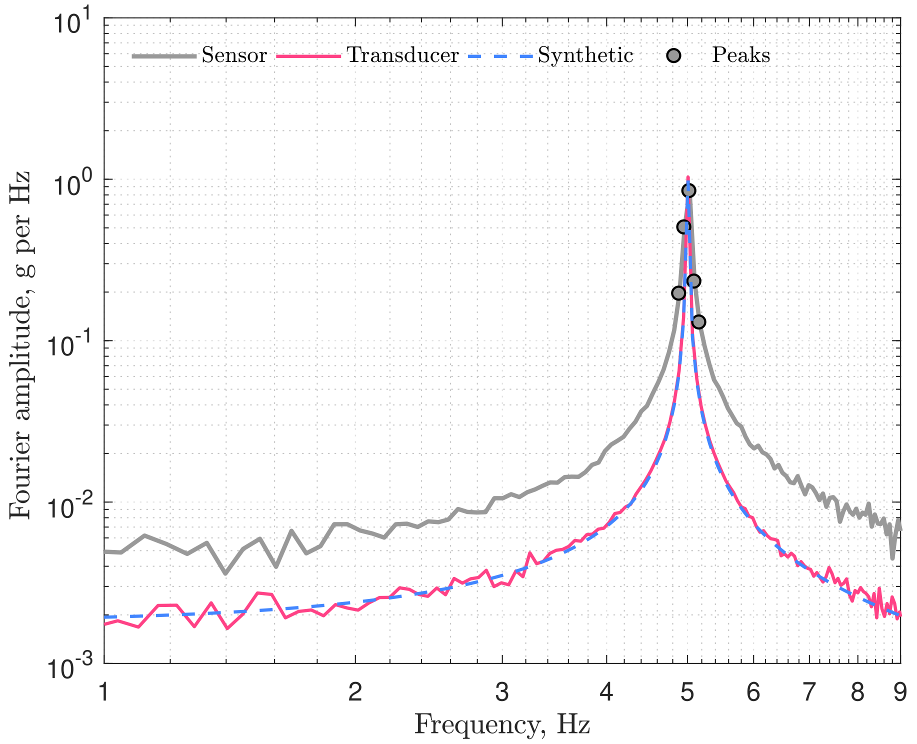

Figure 8: Excerpt of raw data from a sinusoidal input signal of 10 mm nominal amplitude and 5 Hz nominal frequency.

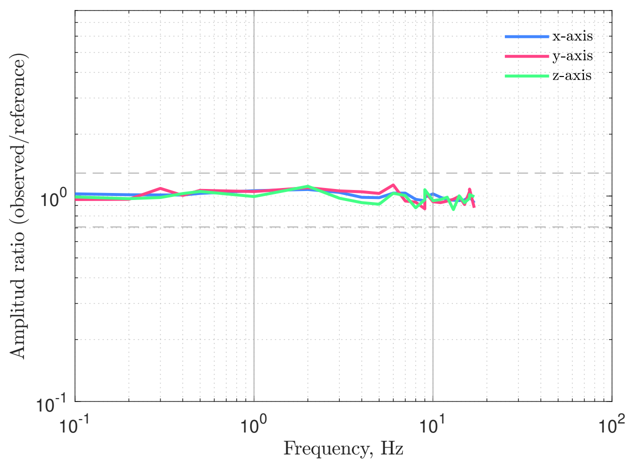

(a)

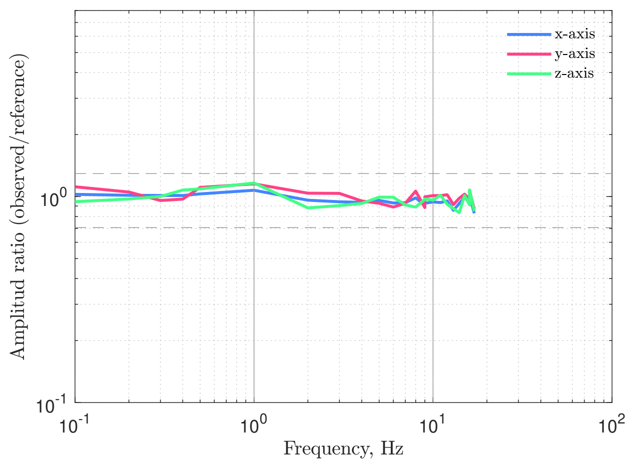

(b)

Figure 9: Computed amplitude ratios versus frequency. The high fidelity transducer is used as a signal reference instead of the synthetic signal input to the dynamic jack. (a) Sensor 1 and (b) Sensor 2

4.4 Clipping behaviour and sensor linearity

The linearity means that there is a linear relationship between the input and output signals [29]. The extent of sensor linearity is usually computed for a given frequency at various levels of amplitude or, in other words, a fixed frequency and variable acceleration. For sensors designed to measure strong ground-motion, a 1% of linearity is commonly accepted as a satisfactory level, as pointed out by [29]. It is interesting to note that the level of linearity is rarely specified, thus making comparison among sensors more difficult. The clipping is a form of distortion in the recorded signal with respect to input signal, once a certain threshold is surpassed. In the case of accelerometers, this threshold is commonly drawn by the mechanical capacity of the sensor, which corresponds to $\pm 3g$ for the MEMS ADXL 335 accelerometer. However, the behaviour of the distortion can vary significantly from sensor to sensor, especially in the case of MEMS as shown by [28], where for instance, some devices actually do not clip the recorded signal but instead blow it up producing highly distorted patterns. The latter inappropriate clipping behaviour is undesirable, and may limit the capacities of the sensor; such as in the double integration processes aiming at obtaining the displacement demand from the recorded acceleration signal, as discussed below in Section 4.5.

To appraise linearity and clipping, the same methodology of inputting sine-wave signals through the linear actuator is used, and response amplitudes are estimated using spectral analysis, as discussed in the previous section. In this case, the input frequency is fixed at 9 Hz, considered to be moderate-to-high in the frequency band of interest, and the amplitude is variable in order to attain a range of acceleration ranging from 0.2g to 3.5g. The smooth clipping behaviour shown by sensor 1 is depicted in Figure 10 for a sequence of increasing accelerations, around the nominal clipping level of the MEMS accelerometer, contrasted to the output signal recorded by the transducer. From Figure 10 a to 10 d, the clipping of the sensor is pointed at the peak of the sine waves, where the sensor output signal tends to flatten whilst the transducer still captures the increase in acceleration of the input wave. A similar smooth clipping behaviour was observed by sensor 2. By computing the amplitude ratios obtained from the tests, through the spectral method, the amplitude ratio versus acceleration levels is assembled and shown in Figure 11, for both tested sensors. The three axis of the sensor clip in a well-behaved manner, as noted by [28], given their smooth attenuation over their nominal clip threshold, that for a sine wave is commonly estimated as the RMS of the signal, which is shown in the plot with a vertical dashed line.

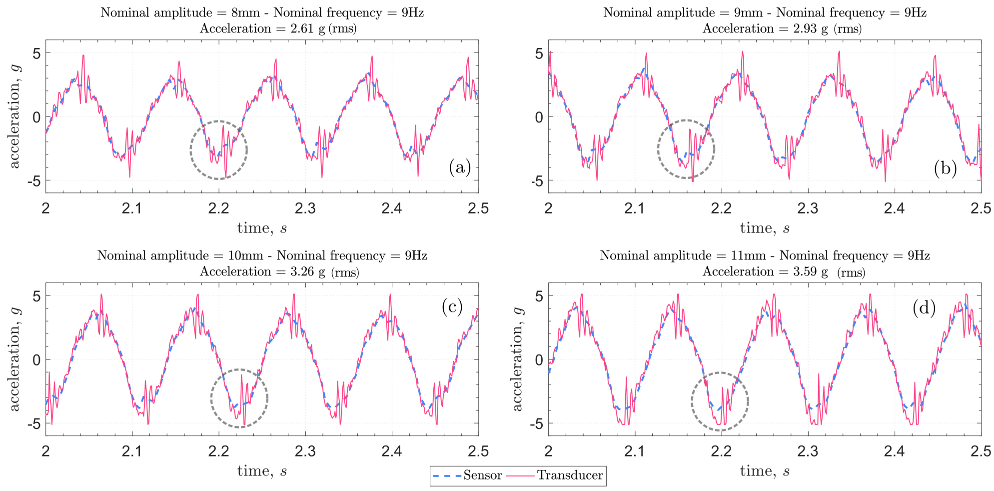

Figure 10: Sequence of tests for accelerations in the neighbourhood of the nominal clipping level of $\pm 3g$ (all excerpts of recorded data correspond to the x-axis of the sensor at fixed nominal 9Hz frequency).

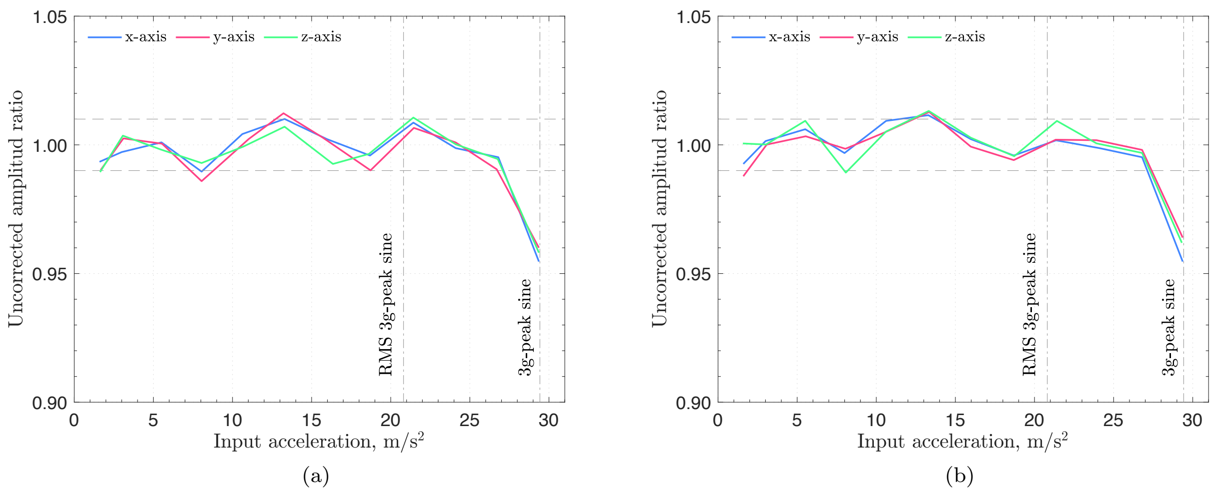

Figure 11: Linearity and clipping for the three axes of the sensor (dashed horizontal lines show $\pm 1\%$ of the expected ratio at unity). (a) Sensor 1 and (b) Sensor 2

4.5 Single and double integration tests

The capability of retrieving permanent or transient displacements from the acceleration recording is paramount during the monitoring of a building or structural system. In earthquake engineering, local drift ratios are typically the most important parameters to appraise the performance of a structure [30], given that they can be readily related to a damage state of the system, which is usually predefined based on the structural configuration of the system. Residual or permanent drifts deserve a special attention given their crucial role in post-earthquake assessment, where structural losses are estimated, and decisions are made based on the state of the structure, such as demolition or retrofitting [31, 32]. Single and double integration process are commonly used to retrieve velocity and displacement time-histories from acceleration recordings, respectively. However, this is an underdetermined problem [28], where usually nonphysical waveforms are obtained for the velocity and displacement. The nature of these spurious results is partially explained by various sources of error, such as unknown boundary conditions for the velocity and displacement, offset of the baseline, and low-frequency noise or artifacts [33, 34]. Several methods have been proposed to individually remedy these sources of error, such as various baseline corrections, filtering and zero-padded sections, among others; some of these are used subsequently below.

The same dynamic tests using sine waves as input signals described in previous sections are used herein. Note that these tests were not designed to induce residual displacements that can later be retrieved, thus the main focus here is to estimate velocity and displacement transient waveforms through time-histories. First, a baseline correction was performed through fitting a cubic polynomial function to the acceleration record, which is subsequently subtracted from the recorded acceleration. Second, zero padded sections are added to the beginning and end of the record, whose adequate length depends on the order and corner frequency of the filter to be applied afterwards [33]. Third, a band-pass Butterworth filter of order 3, and whose corner filter frequencies are 0.1 Hz and 25 Hz, is applied. The lower limit was decided to reflect typical limits of long-period structural systems, whereas the upper limit was chosen based on mechanical noise observed in the collected signals attributed to the actuator operation. Finally, the acceleration record is numerically integrated to obtain the velocity and displacement time-histories. The same methodology was applied to the data collected by the transducer, in order to compare results based on the actual output of the actuator. The results of the single and double integration procedures are shown in Figure 12, for two different levels of nominal amplitude and frequency of the sine wave input signal. In general, step amplitudes and waveforms are well recovered by the sensor, which is an important feature in this exploratory stage, partially due to the stable sample-rate recording. It is noticeable that, for both recovered displacement time-histories, some non-steady behaviour occurs at the beginning of the motion, before reaching a steady state. This behaviour was initially attributed to the processing of the signal; however, the transducer coherently captured this as well, even when different processing methods were used before the integration (e.g., length of the zero-padded regions, and other filters such as Chebyshev). In addition, a similar behaviour was observed consistently for various input signals, thus explained by the control system of the actuator at the beginning of the motion, especially in the case of the highest frequencies tested. Particularly noteworthy is the fact that when residual displacement needs to be retrieved by double-integration of the acceleration record, low-cut filters cannot be used [28]; nevertheless, this needs further consideration in the assessment of the sensor, preferably by having independently-measured offsets or residual displacements in the actual response of structural systems.

5 Seismic Performance of the Prototyped Sensor

This section presents the results of the analyses conducted based on data collected using a shake table to reproduce actual earthquake strong-motion signals. During shake table tests, the sampling ratio of the sensor was set to 200 sps, whereas the transducer or reference sensor recorded the signal at 1000 sps due to the constraints of the data acquisition system. Therefore, to carry out the analysis above-listed in Section 2.1, the acceleration signal recorded by the reference sensor was down-sampled to 200 sps using the Matlab functions "decimate" and "downsample", which deliver identical results when properly tuned. It is worth mentioning that the main difference between these methods is that "decimate" uses a finite impulse response (FIR) low-pass filter before simply down sampling the signal at a sample rate x, equal to 5 herein. The decimate function was used with a filter order of 3.

5.1 Input and response parameters

The main characteristics of the ensemble of earthquake records used in the shake table tests are presented in the following. Figures 13 (a) - (c) show the 5%- damped acceleration response spectra of the three sets of earthquake

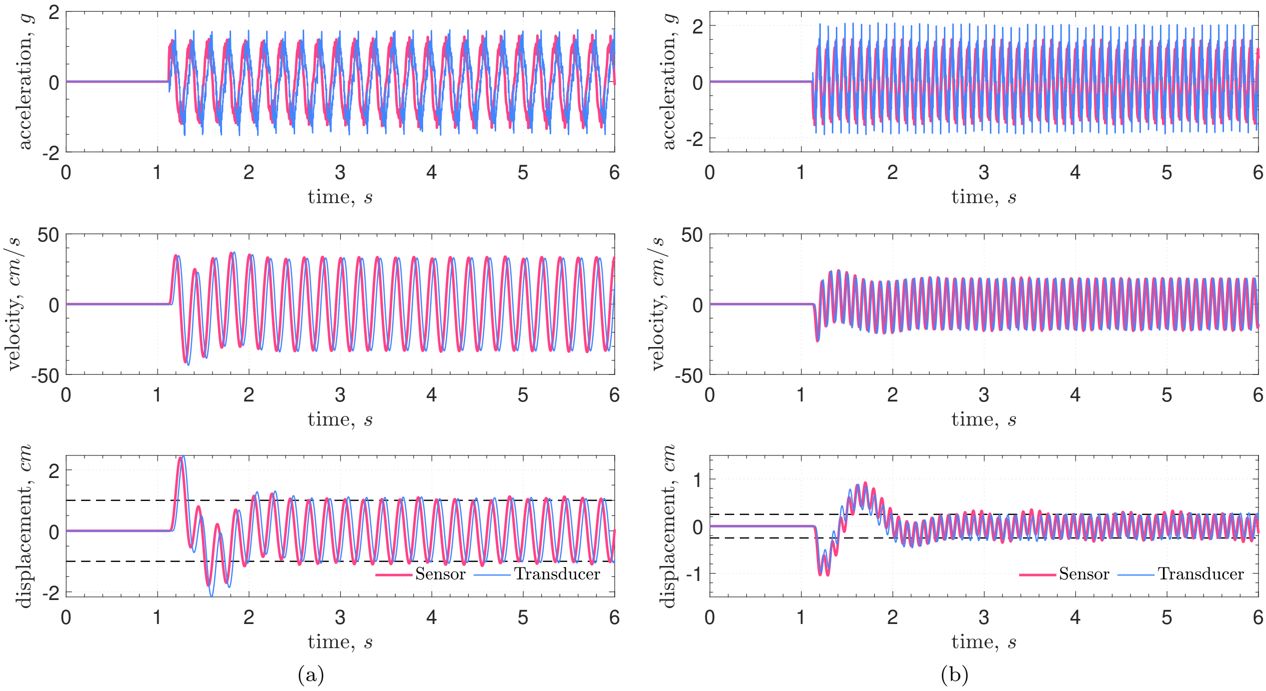

Figure 12: Single and double integration test for 2 input signals: (a) Nominal amplitude = 10 mm and nominal frequency 5 Hz. (b) Nominal amplitude = 2.5mm and nominal frequency 11 Hz. Dashed horizontal lines at bottom panels signal the nominal displacement of input signal.

records, which are categorised as far-field (Set-a), near-field with no velocity pulse (Set-b), and near-field with velocity pulse (Set-c), compounded by 12, 20 and 20 records respectively. The pulse-like ground motions are judged by the wavelet transform analysis classification proposed by [35]. The differences in the response spectral shape are clear, as expected due to the content of frequency and other distinctive key characteristics of far-field and near-field records. The PGA ranges between 0.21g and 0.84g, and the peak ground velocity (PGV) ranges between 19 cm/s and 115 cm/s. The far-field records were recorded at site classes C (very stiff soil sites) and D (stiff soil sites), and the near-field records were recorded at site classes B (rock sites), C, and D; according to the NEHRP site classification [36]. Figure 13 (d) shows the I_A time-history [37] or Husid plots [38] for the entire suite of records, which is used in subsequent analyses as an intensity measure of the records, because it has a particular interest for civil engineers. The latter is due to its capacity to condensate several key ground motion characteristics, such as duration, frequency content and intensity, in a single parameter that serves as a proxy for the destructiveness potential of an earthquake. All selected earthquake records were scaled to match the maximum displacement attainable by the shake table. A summary of source and site data of the ground motions can be seen in Table 2, 3, and 4, for each set of records respectively. The depth and epicentral distance are in Km.

Table 2: Summary of source and site data for the far-field record set

Name of event	**Year**	**Latitude**	**Longitude**	**Depth**	**Magnitude**	**Recording Station**	**Latitude**	**Longitude**	**Distance**
Friuli, Italy	1976	46.345	13.240	5.10	6.5	Tolomezzo	46.382	12.982	20.2
Hector Mine	1999	34.574	-116.291	5.00	7.1	Hector	34.829	-116.335	26.5
Manjil	1990	36.810	49.353	19.00	7.4	Abbar	36.920	48.950	40.4
Northridge	1994	34.231	-118.475	13.09	6.7	Beverly Hills - 12520 Mulhol	34.127	-118.405	13.3
Northridge	1994	34.231	-118.475	13.09	6.7	Canyon Country-WLC	34.419	-118.426	26.5
Maule	2010	-36.170	-73.140	30.10	8.8	Angol	-37.790	-72.710	184.1

The raw time-acceleration signals recorded by the sensor and the reference accelerometer rigidly attached to the surface of the shake table, were firstly processed following the procedure detailed in Section 4.5. Two representative responses are shown in Figure 14 for an individual far-field record and in Figure 15 for a single near-field record, in terms of acceleration, velocity, displacement and FAS. To synchronise the waveforms several methods were used to compare results, and among these the cross-correlation method was selected. This enables the computation of the signals correlation (i.e., maximum equal to 1.0) versus a lag time vector, rendering the lag time corresponding to the largest correlation, which is used to only shift the time of one the waveforms. In general, the sensor produces a good performance with respect to the response of the reference signal, when

Table 3: Summary of source and site data for the near-field with no pulse effects record set

Name of event	Year	Latitude	Longitude	Depth	Magnitude	Recording Station	Latitude	Longitude	Distance
Cape Mendocino	1992	40.334	-124.229	9.60	7.0	Cape Mendocino	40.348	-124.352	10.4
Chi-Chi, Taiwan	1999	23.860	120.800	6.76	7.6	TCU067	22.999	120.184	28.7
Gazli, USSR	1984	40.350	63.470	15.00	6.8	Karakyr	40.350	63.470	12.8
Imperial Valley-06	1979	32.644	-115.309	9.96	6.5	Bonds Corner	32.693	-115.338	6.2
Kocaeli, Turkey	1999	40.727	29.990	15.00	7.5	Yarimca	40.764	29.762	19.3
Imperial Valley-06	1979	32.644	-115.309	9.96	6.5	Chihuahua	32.484	-115.240	18.9
Nahanni, Canada	1985	62.187	-124.243	8.00	6.8	Site 1	62.202	-124.370	6.8
Northridge-01	1994	34.206	-118.554	17.50	6.7	LA - Sepulveda VA	34.249	-118.478	8.5
Nahanni, Canada	1985	62.187	-124.243	8.00	6.8	Site 2	62.234	-124.168	6.5
Loma Prieta	1989	37.041	-121.883	17.48	6.9	Corralitos	37.050	-121.803	7.2

Table 4: Summary of source and site data for the near-field with pulse effects record set

Name of event	Year	Latitude	Longitude	Depth	Magnitude	Recording Station	Latitude	Longitude	Distance
Chi-Chi, Taiwan	1999	23.860	120.800	6.76	7.6	TCU065	24.059	120.691	26.7
Chi-Chi, Taiwan	1999	23.860	120.800	6.76	7.6	TCU102	24.249	120.721	46.5
Duzce	1999	40.775	31.187	10.00	7.1	Duzce	40.844	31.149	1.6
Imperial Valley-06	1979	32.644	-115.309	9.96	6.5	El Centro Array #6	32.839	-115.487	27.5
Imperial Valley-06	1979	32.644	-115.309	9.96	6.5	El Centro Array #7	32.829	-115.504	27.6
Irpinia, Italy-01	1980	40.840	15.28	10.00	6.9	Sturno	41.021	15.115	30.4
Loma Prieta	1989	37.041	-121.883	17.48	6.9	Saratoga - Aloha	37.255	-122.031	27.2
Northridge-01	1994	34.206	-118.554	17.50	6.7	Rinaldi Receiving Sta	34.281	-118.478	10.9
Northridge-01	1994	34.206	-118.554	17.50	6.7	Sylmar - Olive View	34.326	-118.444	16.8
Superstition Hills-02	1987	33.022	-115.831	9.00	6.5	Parachute Test Site	32.929	-115.701	16

assessed in terms of wave form, PGA, PGV and Peak Ground Displacement (PGD). This remains valid in the computation of FAS, where the sensor performs well, capturing amplitude and distribution of frequency. A closer look is shown in Figure 16 where both waveforms are superimposed with a zoom in on the time and frequency range respectively.

The same pair of records used above for assessing the time-history response, are used herein to appraise the 5%-damped acceleration response spectrum and I_A through Husid plots. In general, the response spectrum of the sensor behaves well when compared to the reference signal, as shown in Figure 17 (a) and (c) for a far-field and near-field record respectively. In contrast, there is a poorer sensor performance during the computation of I_A, whose selected results are presented in Figures 17 (b) and (d). In general, the sensor tends to underestimate the I_A of the recording with respect to the value reported by the reference signal. Given that the computation of I_A involves the numerical time-integral of the whole acceleration signal (i.e., $I_A = \frac{\pi}{2g}\int_0^{T_d} a(t)^2 dt$), there seems to be an accumulated error of the small differences in individual acceleration peaks (positive and negative) between the sensor and reference signal. Although the reference signals used in these analyses, correspond to a down-sampled one (i.e., 200 sps) in order to properly compare to the sensor signal, if the sensor sampling rate is increased, the computation of the I_A improves. However, as discussed above, the control of the sensor can be easily modified to increase the sampling rate of one specific axis at the cost of reducing the sampling rate of the others, because of the micro-controller processing capacity.

5.2 Errors in acceleration signal, Arias Intensity and spectral response

The computation of ground motion intensity measures are generally based on the whole processed recorded signal of acceleration, therefore it is relevant to quantify the quality of the full time-history acceleration recording, in contrast to solely individual peak values. To this end, the mean squared error (MSE) of the acceleration recorded by the sensor with respect to the reference signal was computed as follows:

$$MSE(a_{sensor}) = \frac{\sum_{i=1}^{N}[a_{sensor}(t_i) - a_{reference}(t_i)]^2}{N} \quad (2)$$

Where a_{sensor} and $a_{reference}$ are the acceleration time-history recorded by the sensor and transducer respectively for an individual ground motion record. N corresponds to the number of samples recorded in the signal. To prevent small peaks controlling the results (i.e., non strong-motion or pseudo motionless sensing), only acceleration peaks above an amplitude cut off corresponding to 0.2 times the PGA was used to compute MSE. The results are shown in Figure 18 (a) as a function of the PGA of the ground motion record. The minimum computed MSE value was $4.088x10^{-3}g^2$, and the maximum reached $0.021g^2$. Most of the values are concentrated towards the lower end, however for seven individual earthquakes, the MSE exceeds $0.01g^2$, which is a

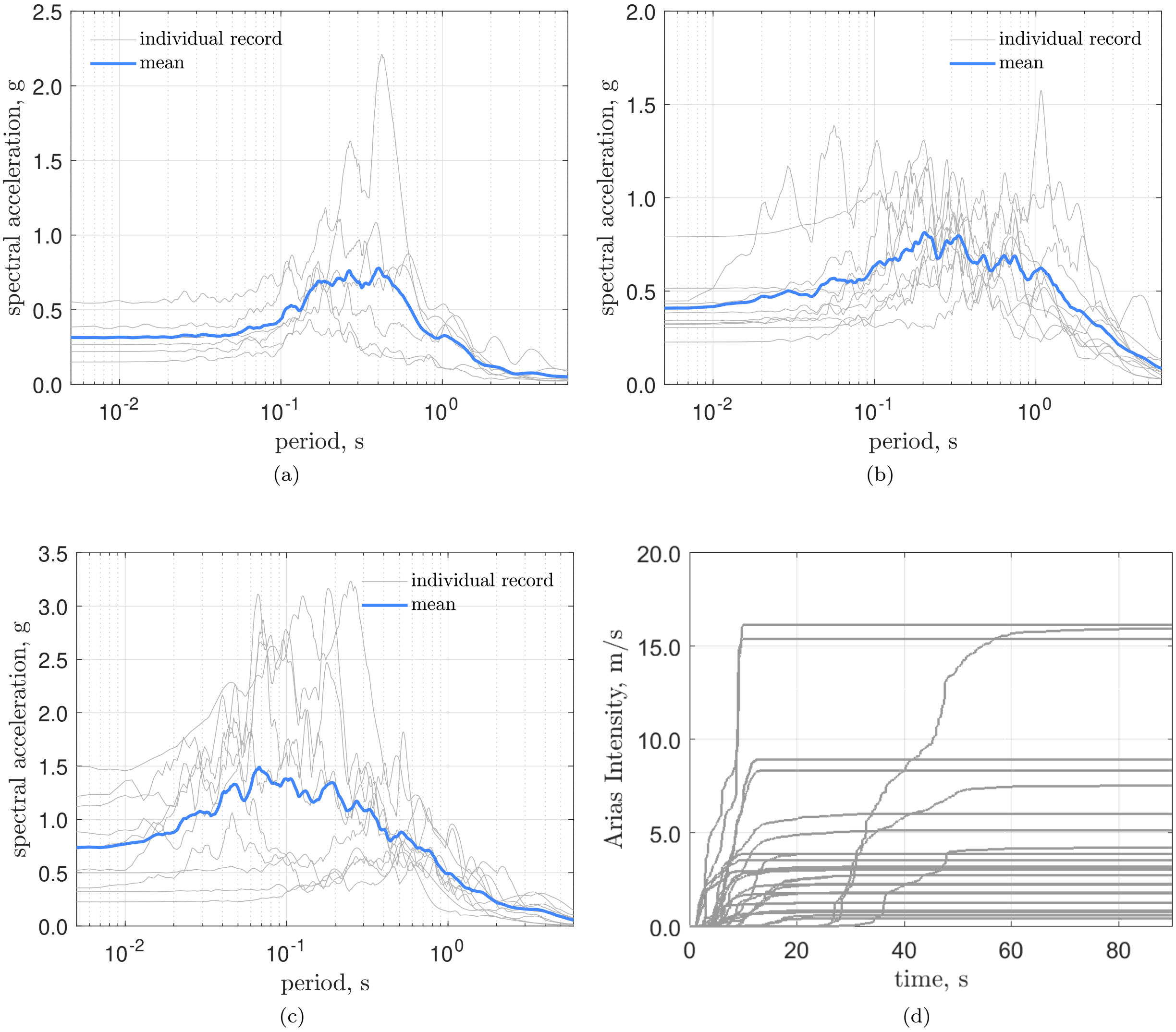

Figure 13: 5%- damped acceleration response spectra of the input motion of: (a) Set-a of far-field records (b) Set-b of near-field records with no-pulse (c) Set-c of near-field records with pulse. Subfigure (d) shows cumulative Arias Intensity time-history for all input motions.

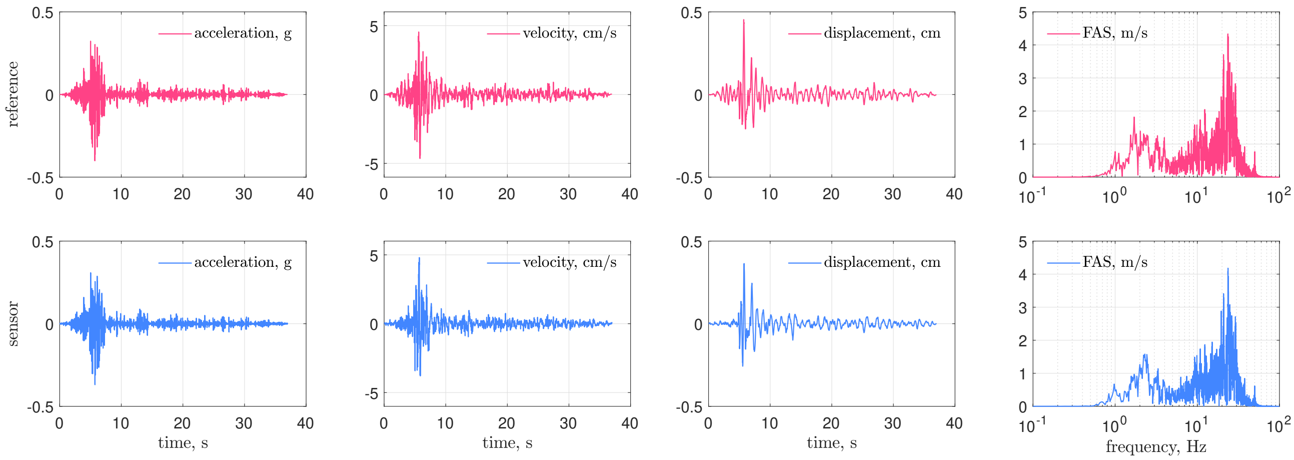

Figure 14: Time-history response and FAS of a representative record from Set-a recorded with the prototyped sensor and transducer referred to as 'reference'. Input motion is Cape Mendocino 04/25/92 1806, Rio del overpass FF, 270 (CDMG Station 89324).

common upper limit for higher fidelity sensors.

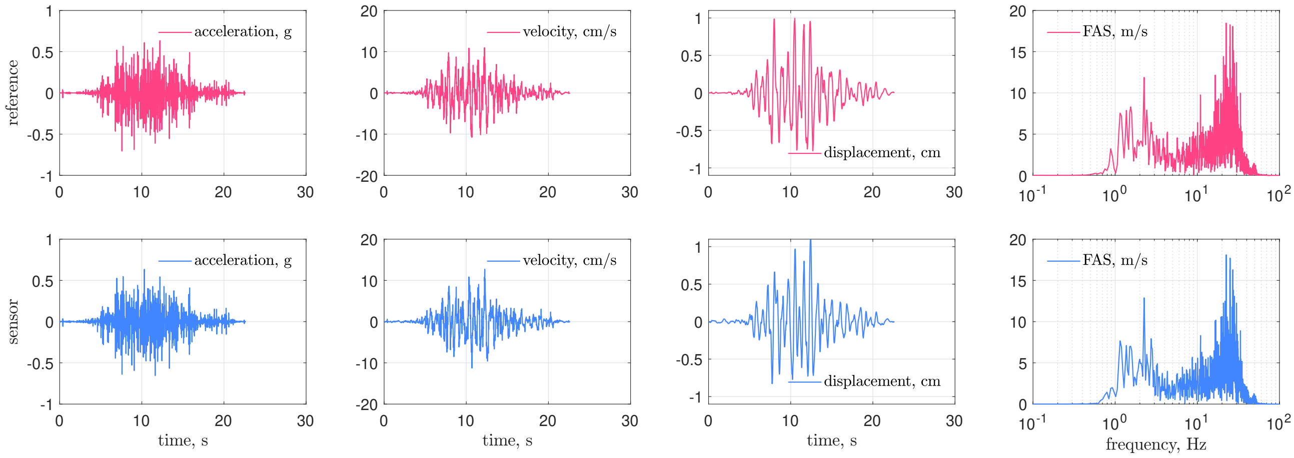

Figure 15: Time-history response and FAS of a representative record from Set-c recorded with the prototyped sensor and transducer referred to as 'reference'. Input motion is Irpina, Italy 11/23/1980, (Sturno Station, 270).

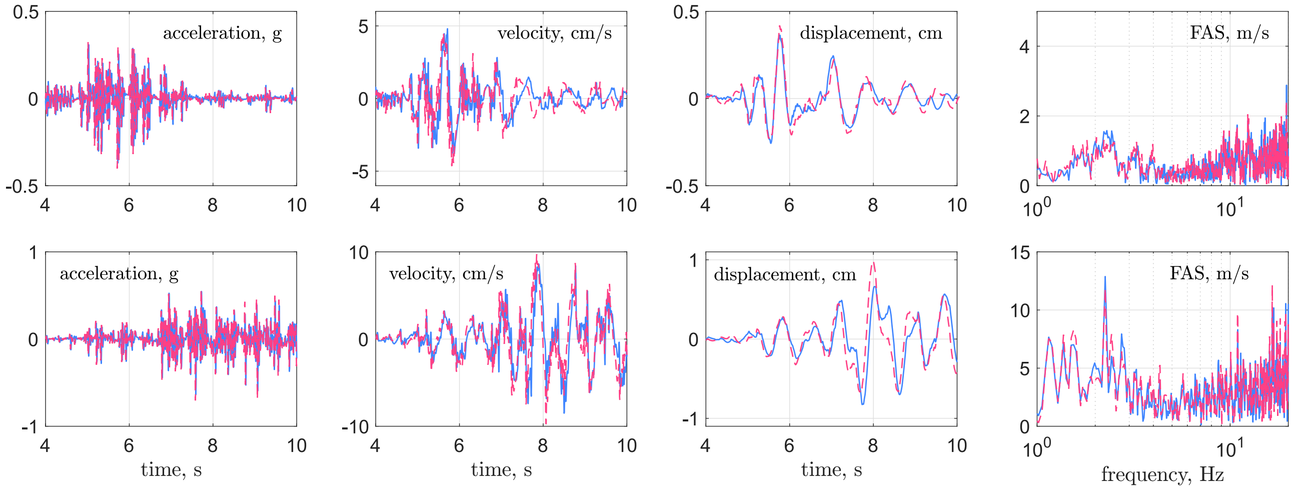

Figure 16: Zoom in on time-history and FAS response. Top panels correspond to far-field record considered in Figure 14 and bottom panels correspond to near-field record considered in Figure 15. Solid blue line for the sensor and dashed red line for the transducer.

Regarding the error in the computation of I_A, first it is important to mention that several earthquake intensity measures, such as $S_a(T)$ and I_A are approximately log-normally distributed (e.g., [39, 40]). Hence, the error in I_A obtained from the sensor signal with respect to the reference signal, is computed in logarithmic space, as follows:

$$Error_{I_A} = log(\frac{I_{A_{sensor}}}{I_{A_{reference}}}) \tag{3}$$

The errors in $log(I_A)$ results are shown in Figure 18 (c) as a function of PGA for the whole ensemble of ground-motions tested. In general there is a flat behaviour of the error across the PGA levels considered in the study, with an average absolute error around 0.07 log(m/s), and one outlier point that reached 0.16 log(m/s). These errors show a small magnitude, and their uniform flat behaviour with regard to PGA can be used to quantify their general magnitude and trend in order to make correction in the calculation of I_A.

With respect to the error in the computation of the ordinates of the acceleration response spectrum, a more probabilistic approach may be considered. The difference between the 5%− damped acceleration response spectra computed from the sensor and the reference data, may be quantified through the "goodness-of-fit" method presented by [41]. These can shed some light on the sensor's bias and uncertainty. Thus, if a model is assumed, the residual r (i.e., observed - predicted), is defined as follows:

$$r_{im}(T_k) = log(S^{ref}_{A_{im}})(T_k) - log(S^{sensor}_{A_{im}}(T_k)) \tag{4}$$

Where T_k is the period used to calculate the ordinates of the acceleration response spectrum $S^{ref}_{A_{im}}(T_k)$, and

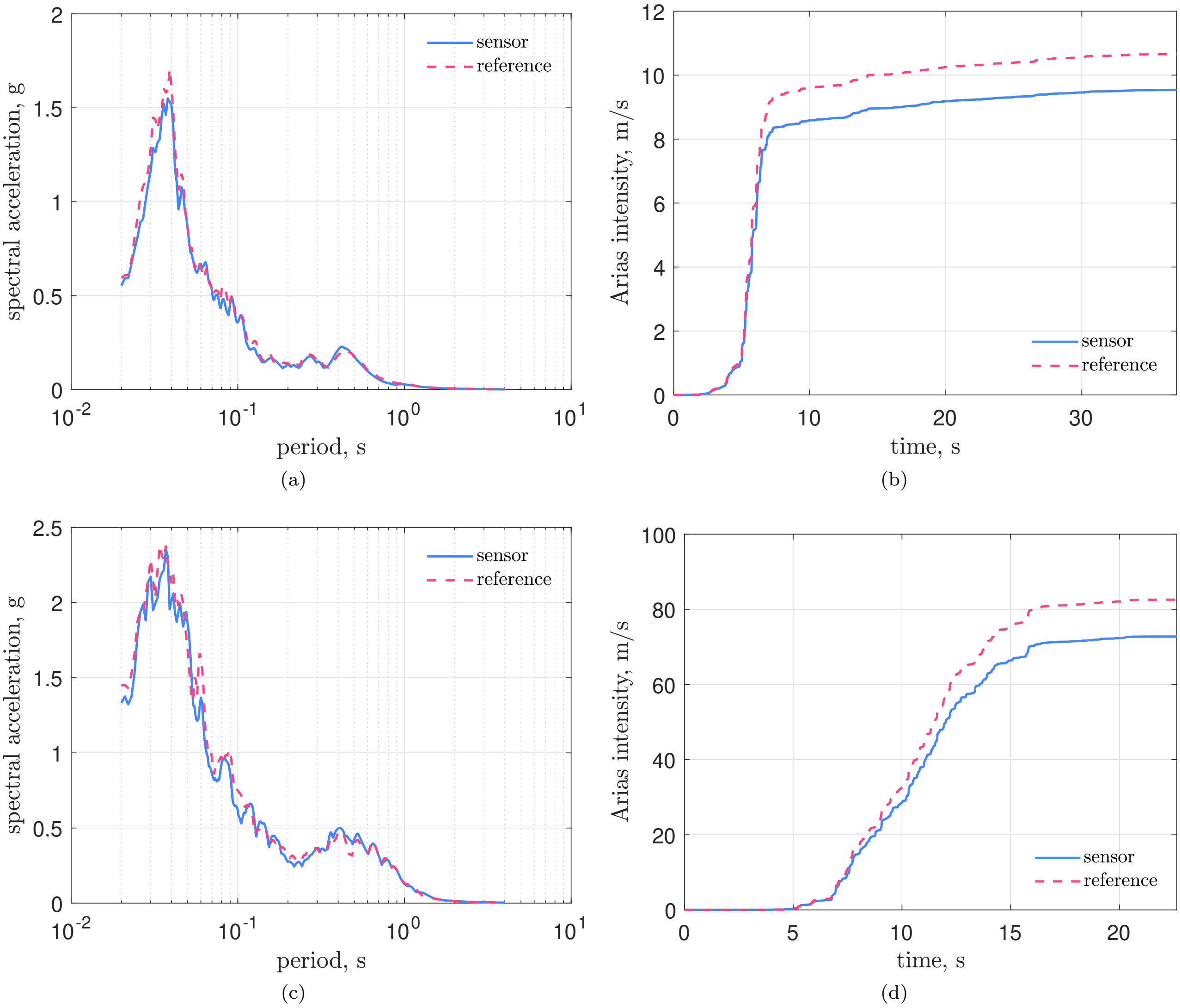

Figure 17: 5%- damped acceleration response spectra and Husid plots. Top panel: Cape Mendocino 04/25/92 1806, Rio del overpass FF, 270 (CDMG Station 89324), and bottom panel: Irpina, Italy 11/23/1980, (Sturno Station, 270).

$S_{A_{im}}^{sensor}(T_k)$; k is the period index, i is the earthquake index, and m is the component of the motion. Given r_{im}, the bias can be estimated at each considered period T_k, as follows:

$$bias(f_k) = \frac{\sum_{i=1}^{N_i} r_{im}(f_k)}{N_m N_i} \tag{5}$$

In this particular case, N_i is the number of tests per given strong-motion, and N_m is the number of ground-motion components considered, which in this cases is equal to unity. Thus, the variance in the error term and the standard error of the bias may be estimated as follows:

$$\sigma^2_{sensor}(f_k) = \frac{\sum_{i=1}^{N_i} [r_{im}(f_k) - bias(f_k)]^2}{N_i - 1} \tag{6}$$

$$\sigma_{bias}(f_k) = \frac{\sqrt{\sigma^2_{sensor}(f_k)}}{\sqrt{N_i}} \tag{7}$$

Figure 18 (c) shows the computed bias in the 5% damped acceleration response spectrum using the 54 earthquakes records, as a function of period (i.e., T_k). The absolute maximum bias estimated corresponds to 0.045 log(g), and exhibits a relatively flat behaviour across the periods considered to obtain bias, variance and standard error of the bias.

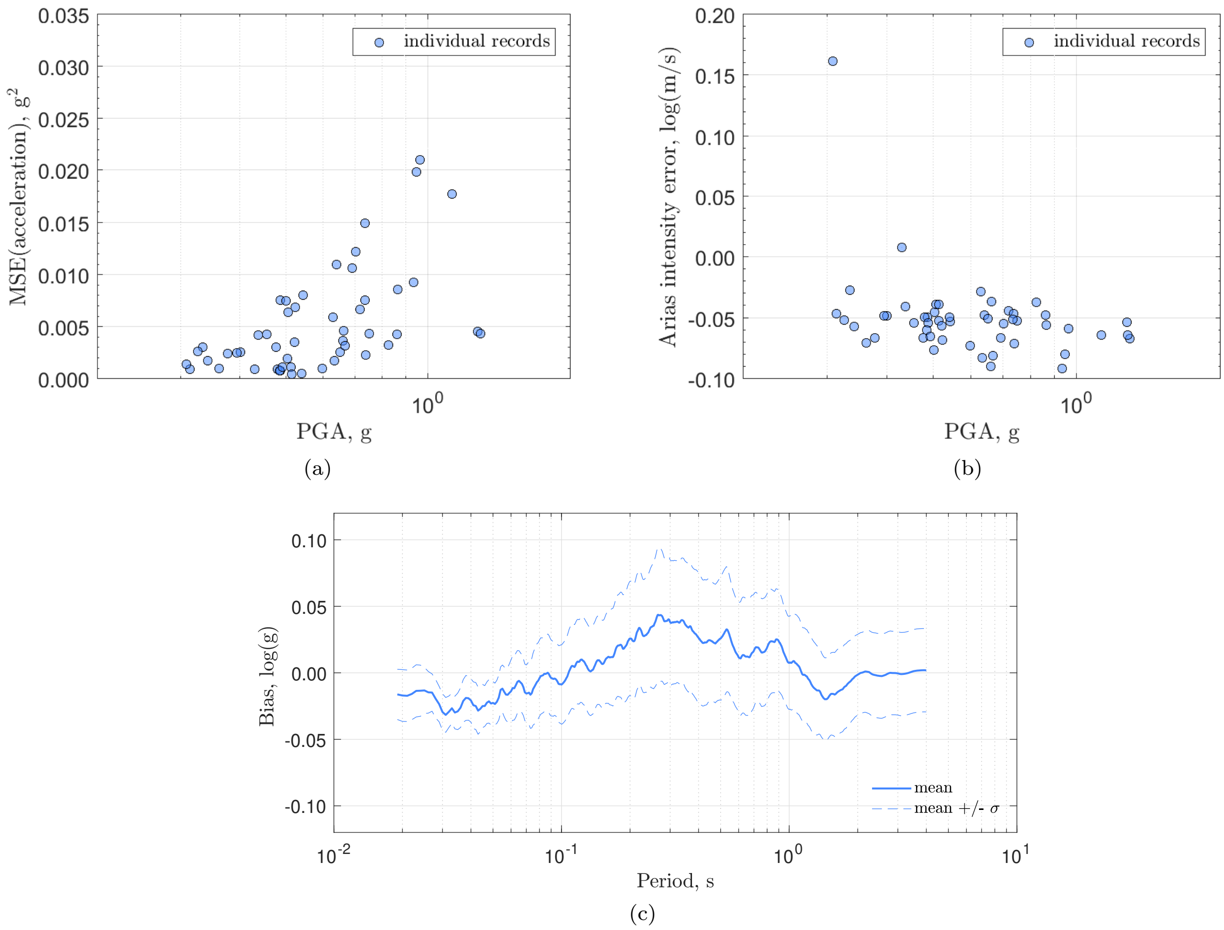

Figure 18: (a) Mean Squared Error (MSE) of acceleration records versus PGA for all individual input motions tested in the shaking table. (b) Error in the computation of the Arias Intensity ($log(A_I)$) versus PGA for all individual input motions tested in the shaking table. (c) Bias and standard error in 5% damped acceleration response spectra for all tested ground-motion records.

5.3 Data reliability

To investigate and quantify the reliability of the data that can be recorded by the sensor, two ground-motion records from the tests conducted above were selected and subsequently used in the linear shake table. Each individual record was repeated 7 times, in order to assess the scattering and robustness of the sensor in the calculation of MSE of the time-acceleration series, the half-length of 90% confidence interval, and the "goodness-of-fit" of the response spectral acceleration. Figure 19 shows the acceleration response spectra obtained for both repeated pairs of earthquake records, along with the mean and standard deviation of spectral ordinates considering all seven samples. The bottom panels in Figure 19 show the bias of the spectral accelerations, computed by means of Equation 5. To calculate the MSE of time-acceleration series recorded by the sensor with respect to the reference signal, Equation 2 is used. The reliability of the collected experimental data, at any given time t_i, is estimated through the probability β of the mean value (m_{sensor}) of the accelerations recorded by the sensor (a_{sensor}) to be within the confidence interval of length $2b$ which is centered at the acceleration of the reference signal $a_{reference}$ for a given time t_i [42, 43], expressed as follows:

$$\beta = P[a_{reference} - b \leq m_{sensor} \leq a_{reference} + b] \tag{8}$$

To undertake this analysis, the following assumptions are considered [43]:

1. All experiments are conducted under identical conditions, hence implying that the expected value $\mathrm{E}(a_{sensor-i}) = \mathrm{E}(a_{sensor})$ and standard deviation $\sigma_{sensor-i} = \sigma_{sensor}$ are identical in all cases, with $i = 1, 2, ..., 7$.

2. No mutually independent relationship between results, which means bias can be ignored. Hence all the expected values $\mathrm{E}(a_{sensor})$ are equal to a constant parameter m_{sensor}.

3. All experimental results follow a normal distribution, indicating that the mean values of the seven a_{sensor} measurements at any given time t_i follow a normal distribution. (i.e., $\bar{a}_{sensor} = (\sum_{i=1}^{n} a_{sensor-i})(1/n)$ with n=7).

4. It was assumed that the low-cost sensor and the reference sensor were recording an identical signal, given that no differential motions across the shake table were observed, mostly due to the small dimensions of the table.

Based on the above assumptions a new random variable can be defined, which follows a Student's t distribution with $n-1$ degrees of freedom [44, 43] expressed as follows:

$$T = \frac{(\bar{a}_{sensor} - m_{sensor})\sqrt{n}}{a_{sensor}} \tag{9}$$

Assuming that T_{N-1} can represent the cumulative distribution, then by replacing m_{sensor} in Equation 8 by T in Equation 9, the confidence interval can be solved through the following equations:

$$\beta = P[x_1 \leq T \leq x_2] = T_{N-1}(x_2) - T_{N-1}(x_1) \tag{10}$$

$$x_1, x_2 = \frac{(\bar{a}_{sensor} - a_{reference} \pm b)\sqrt{n}}{\sigma_{sensor}} \tag{11}$$

Where b is the half-length of the confidence interval. Thus, Equation 10 can be solved numerically in order to obtain b_i, for any given time t_i. Moreover, a time independent average index of b_i can be used by computing the average across the entire acceleration time-series: $\bar{b} = (1/N)\sum_{i=1}^{N}(b_i)$ [42]. These two indexes convert the information embedded in the measurements into a single metric, enabling a comparison between the low-cost sensor signal and the reference signal from the transducer. For the sake of brevity, Table 5 shows the estimated half-width $\bar{b}$ of the 90% confidence interval, whose magnitudes are moderate.

Table 5: Averaged half-length of 90% confidence interval for both considered earthquake records measurements

Metric	Earthquake 1	Earthquake 2
$\bar{b}$	$0.0813g$	$0.0897g$
MSE_{acc}	$0.0075g^2$	$0.008g^2$

6 Concluding Remarks

An open-source low-cost sensing system for recording accelerations has been proposed in this study and its performance has been assessed through a series of comparative validation tests. The sensor has been entirely built from off-the-shelf electronic components, whose construction and controlling guidelines will be provided as an open-source platform which will be continuously updated.

The assessments carried out in this investigation suggest that the proposed sensing technique is suitable for deployment as an accelerometer for seismic monitoring of structural systems. Based on standardised tests, the results demonstrate low levels of self-noise, considering the nature of the MEMS analogue accelerometer embedded in the sensor. The amplitude transfer functions exhibit a flat behaviour for the full range of frequencies tested, whose boundaries were limited by the installed capacity within the laboratory. However, this flat behaviour is expected to be coherent up to the resonant frequency of the MEMS accelerometer, whose absolute value is much higher than the bandwidth of frequencies of interest for seismologists and structural earthquake engineers. The clipping tests indicate a flat behaviour (i.e., high linearity) of the amplitude transfer function from low acceleration levels, up to the vicinity of the maximum nominal recordable acceleration of $\pm 3g$, at which a typical roll-off is observed. Under long-time operations, the micro-controller exhibits a robust performance, maintaining a steady pace of sampling. The reliability of the sensor under non-stationary excitations was examined and quantified by testing over 50 strong-motion recordings from actual earthquakes in a linear shake table. In general, the sensor was shown to produce good performance in terms of measuring strong-motion intensity metrics, such as PGA, PGV and PGD. An average MSE of the full time-acceleration series of 0.0036 g^2 was obtained when compared to the data observed by the reference accelerometer. Spectral acceleration ordinates were found to be in a close match with the accelerations reported by the reference signal, with a horizontal spectral acceleration bias within 0.025 - 0.045 $log(g)$ and relatively flat across the range of periods under consideration. Less accurate estimations were however obtained for the computation of I_A, where the

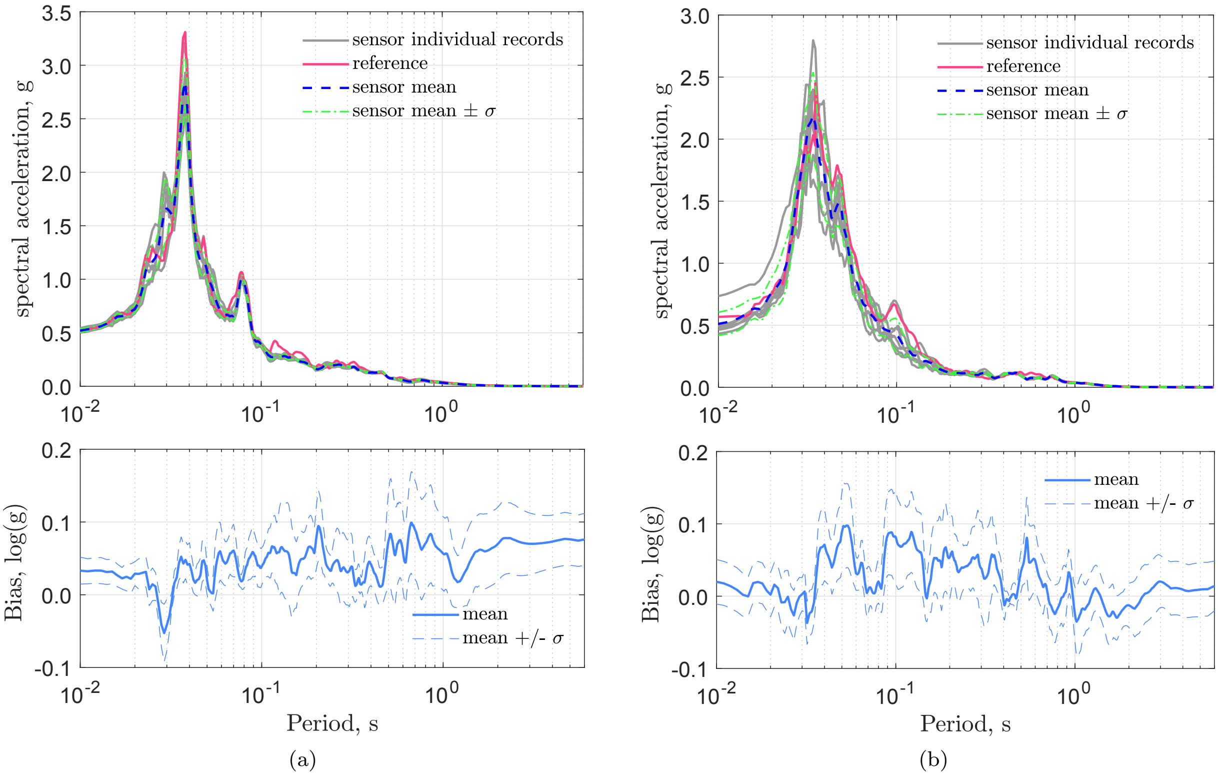

Figure 19: 5%- damped acceleration response spectra for the pairs of repeated input motion selected to conduct the reliability analyses.

sensor underestimated the magnitudes. The half-width of the 90% confidence interval was used to quantify the reliability of the measurements, and a moderate average value of 0.086 g was obtained.

The work carried out within this study opens the door for several future prospects and further natural developments of this type of sensing techniques, towards obtaining a standalone real-time data collection sensor. The sensor performance could be improved by testing a wider range of MEMS accelerometers, particularly aiming at covering a wider range of absolute acceleration and reducing the self-noise levels. Future efforts will be focused towards the advancement in connectivity and communication protocols, power supply possibilities, and general maintenance procedures of an autonomous operating sensor.

Acknowledgments

The support of the Earthquake Engineering Field Investigation Team (EEFIT) and the Institution of Structural Engineers, through the 2018 EEFIT Research Grant Scheme, is gratefully acknowledged. We also thank the three anonymous reviewers whose detailed and insightful comments and suggestions helped improve and clarify the contents of this publication.

References

[1] Elizabeth S Cochran. To catch a quake. *Nature communications*, 9(1):2508, 2018.

[2] Robert W Clayton, Thomas Heaton, Mani Chandy, Andreas Krause, Monica Kohler, Julian Bunn, Richard Guy, Michael Olson, Mathew Faulkner, MingHei Cheng, et al. Community seismic network. *Annals of Geophysics*, 54(6), 2012.

[3] Elizabeth S Cochran, Jesse F Lawrence, Carl Christensen, and Ravi S Jakka. The quake-catcher network: Citizen science expanding seismic horizons. *Seismological Research Letters*, 80(1):26–30, 2009.

[4] Shigeki Horiuchi, Yuko Horiuchi, Shunroku Yamamoto, Hiromitsu Nakamura, Changjiang Wu, Paul A Rydelek, and Masaaki Kachi. Home seismometer for earthquake early warning. *Geophysical Research Letters*, 36(5), 2009.

[5] Yih-Min Wu. Progress on development of an earthquake early warning system using low-cost sensors. *Pure and Applied Geophysics*, 172(9):2343–2351, 2015.

[6] A D'Alessandro. Tiny accelerometers create Europe's first urban seismic network. *Eos*, 97(10.1029), 2016.

[7] Christos Z Karakostas, Vassilis K Papanikolaou, and Nikolaos P Theodoulidis. An ultra-dense strong-motion urban network based on in-house designed mems accelerographs: the case of Lefkada city, Greece. In *16th European Conference on Earthquake Engineering*, 2018.

[8] BA Brooks, JC Baez, T Ericksen, SE Barrientos, SE Minson, C Duncan, C Guillemot, D Smith, M Boese, ES Cochran, et al. Smartphone-based earthquake and tsunami early warning in Chile. In *AGU Fall Meeting Abstracts*, 2016.

[9] Qingkai Kong, Richard M Allen, Louis Schreier, and Young-Woo Kwon. MyShake: A smartphone seismic network for earthquake early warning and beyond. *Science advances*, 2(2):e1501055, 2016.

[10] BC Christensen and JF Blanco Chia. Raspberry Shake-A World-Wide Citizen Seismograph Network. In *AGU Fall Meeting Abstracts*, 2017.

[11] Robert E Anthony, Adam T Ringler, David C Wilson, and Emily Wolin. Do low-cost seismographs perform well enough for your network? An overview of laboratory tests and field observations of the OSOP Raspberry Shake 4D. *Seismological Research Letters*, 90(1):219–228, 2018.

[12] Mehmet Çelebi. Recorded earthquake responses from the integrated seismic monitoring network of the Atwood Building, Anchorage, Alaska. *Earthquake Spectra*, 22(4):847–864, 2006.

[13] Monica D Kohler, Thomas H Heaton, and Samuel C Bradford. Propagating waves in the steel, moment-frame factor building recorded during earthquakes. *Bulletin of the Seismological Society of America*, 97(4):1334–1345, 2007.

[14] Chiara Bedon, Enrico Bergamo, Matteo Izzi, and Salvatore Noè. Prototyping and validation of MEMS accelerometers for structural health monitoring—The case study of the Pietratagliata cable-stayed bridge. *Journal of Sensor and Actuator Networks*, 7(3):30, 2018.

[15] Alessandro Sabato. Pedestrian bridge vibration monitoring using a wireless MEMS accelerometer board. In *2015 IEEE 19th International Conference on Computer Supported Cooperative Work in Design (CSCWD)*, pages 437–442. IEEE, 2015.

[16] Hidehiko Sekiya, Kentaro Kimura, and Chitoshi Miki. Technique for determining bridge displacement response using MEMS accelerometers. *Sensors*, 16(2):257, 2016.

[17] Guang-Dong Zhou and Ting-Hua Yi. Recent developments on wireless sensor networks technology for bridge health monitoring. *Mathematical Problems in Engineering*, 2013, 2013.

[18] A Holovatyy, V Teslyuk, M Iwaniec, and M Mashevska. Development of a system for monitoring vibration accelerations based on the Raspberry Pi microcomputer and the ADXL1345 accelerometer. *Eastern-European Journal of Enterprise Technologies*, 6(9):52–62, 2017.

[19] Shamim N Pakzad, Gregory L Fenves, Sukun Kim, and David E Culler. Design and implementation of scalable wireless sensor network for structural monitoring. *Journal of infrastructure systems*, 14(1):89–101, 2008.

[20] Manuel Ruiz-Sandoval, Tomonori Nagayama, and BF Spencer Jr. Sensor development using Berkeley Mote platform. *Journal of Earthquake Engineering*, 10(02):289–309, 2006.

[21] Maurice A Biot. *Transient oscillations in elastic systems*. PhD thesis, California Institute of Technology, 1932.

[22] Eduardo Miranda, Athanasia K Kazantzi, and Dimitrios Vamvatsikos. New approach to the design of acceleration-sensitive non-structural elements in buildings. In *16th European Conference on Earthquake Engineering*, pages 18–21, 2018.

[23] Advanced National Seismic System. ANSS, Working Group. Instrumentation Guidelines for the Advanced National Seismic System [Working group on instrumentation, siting, installation, and site metadata of the Advanced National Seismic System technical integration committee]. Technical Report Version 1.0, Geological, Survey, 2008.

[24] Peter W Rodgers. Frequency limits for seismometers as determined from signal-to-noise ratios. Part 1. The electromagnetic seismometer. *Bulletin of the Seismological Society of America*, 82(2):1071–1098, 1992.

[25] Peter Welch. The use of fast Fourier transform for the estimation of power spectra: a method based on time averaging over short, modified periodograms. *IEEE Transactions on audio and electroacoustics*, 15(2):70–73, 1967.

[26] John F Clinton and Thomas H Heaton. Potential advantages of a strong-motion velocity meter over a strong-motion accelerometer. *Seismological Research Letters*, 73(3):332–342, 2002.

[27] Antonino D'Alessandro, Giovanni Vitale, Salvatore Scudero, Roberto D'Anna, Antonio Costanza, Adriano Fagiolini, and Luca Greco. Characterization of MEMS accelerometer self-noise by means of PSD and Allan Variance analysis. In *2017 7th IEEE International workshop on advances in sensors and interfaces (IWASI)*, pages 159–164. IEEE, 2017.

[28] JR Evans, Richard M Allen, AI Chung, ES Cochran, Richard Guy, M Hellweg, and JF Lawrence. Performance of several low-cost accelerometers. *Seismological Research Letters*, 85(1):147–158, 2014.

[29] Jens Havskov and Gerardo Alguacil. *Instrumentation in earthquake seismology*, volume 358. Springer, 2004.

[30] M Çelebi. Real-time monitoring of drift for occupancy resumption. In *Proc. 14th World Conference on Earthquake Engineering (14WCEE)*, 2008.

[31] MA Bravo-Haro and AY Elghazouli. Permanent seismic drifts in steel moment frames. *Journal of Constructional Steel Research*, 148:589–610, 2018.

[32] Gregory A MacRae and Kazuhiko Kawashima. Post-earthquake residual displacements of bilinear oscillators. *Earthquake engineering & structural dynamics*, 26(7):701–716, 1997.

[33] David M Boore. On pads and filters: Processing strong-motion data. *Bulletin of the Seismological Society of America*, 95(2):745–750, 2005.

[34] David M Boore and Julian J Bommer. Processing of strong-motion accelerograms: needs, options and consequences. *Soil Dynamics and Earthquake Engineering*, 25(2):93–115, 2005.

[35] Jack W Baker. Quantitative classification of near-fault ground motions using wavelet analysis. *Bulletin of the Seismological Society of America*, 97(5):1486–1501, 2007.

[36] FEMA. NEHRP recommended provisions for seismic regulations for new buildings and other structures. Technical report, FEMA, 2003.

[37] Arturo Arias. Measure of earthquake intensity. Technical report, Massachusetts Inst. of Tech., Cambridge. Univ. of Chile, Santiago de Chile, 1970.

[38] Raúl Husid. Características de terremotos. Análisis general. *Revista IDIEM*, 8(1):ág–21, 1969.

[39] William B Joyner and David M Boore. Measurement, characterization, and prediction of strong ground motion. In *Earthquake Engineering and Soil Dynamics II, Proceedings of American Society of Civil Engineers Geotechnical Engineering Division Specialty Conference, Park City, Utah*, pages 43–102, 1988.

[40] Nicolas Luco and C Allin Cornell. Structure-specific scalar intensity measures for near-source and ordinary earthquake ground motions. *Earthquake Spectra*, 23(2):357–392, 2007.

[41] NA Abrahamson. Uncertainty in numerical strong motion predictions. In *Proc. Fourth US Nat. Conf. Earthq. Eng.*, volume 1, pages 407–416, 1990.

[42] Shideh Dashti, Jonathan D Bray, Jack Reilly, Steven Glaser, Alexandre Bayen, and Ervasti Mari. Evaluating the reliability of phones as seismic monitoring instruments. *Earthquake Spectra*, 30(2):721–742, 2014.

[43] Radu Popescu and Jean H Prevost. Comparison between VELACS numerical 'class A'predictions and centrifuge experimental soil test results. *Soil Dynamics and Earthquake Engineering*, 14(2):79–92, 1995.

[44] Jack R Benjamin and C Allin Cornell. *Probability, statistics, and decision for civil engineers*. Courier Corporation, 2014.